HOKKAIDO UNIVERSITY

Title	Dynamic equilibrium state of a Cooling Induced Current in the Japan Sea
Author(s)	Fang, Xiaorong; Isoda, Yutaka
Citation	北海道大学水産科学研究彙報, 70(1), 25-40
Issue Date	2020-08-24
DOI	https://doi.org/10.14943/bull.fish.70.1.25
Doc URL	https://hdl.handle.net/2115/79114
Type	departmental bulletin paper
File Information	bull.fish.70.1.25.pdf

Hokkaido University Collection of Scholarly and Academic Papers : HUSCAP

Bull. Fish. Sci. Hokkaido Univ.
70(1), 25–40, 2020.
DOI 10.14943/bull.fish.70.1.25

Dynamic equilibrium state of a Cooling Induced Current in the Japan Sea

Xiaorong FANG[1] and Yutaka ISODA[2]

(Received 23 October 2019, Accepted 16 December 2019)

Abstract

A multi-layered numerical model driven by seasonal change in sea surface heat flux with excess cooling was used to investigate the dynamics of a cooling induced current (CIC) in the Japan Sea. The original idea of the CIC was proposed by Isoda (1999) (*Journal of Oceanography*, **55**, 585–596) as follows : eastward thermal flow in the interior region, i.e., Tsushima Warm Current (TWC), accompanied with meridional thermal gradient on the planetary-β plane would be determined by the heat balance between net heat loss at the sea surface and lateral heat transport from the southern entrance into the Japan Sea. The CIC model produced a significant meandering TWC with an east-west wave number of three, based on the property of a standing Rossby wave, only under the model condition that coexisted with seasonal disturbances of heat. A positive heat supply from the southern entrance to the Japan Sea occurred in late winter, extended slowly to the TWC region as the offshore advection of meandering patchiness in summer, and then contributed to the heat loss by sea surface cooling in the following winter. The whole TWC region was cooled not only at the sea surface in winter, but also by eastward advection of upwelled cold waters originating from the western boundary area in summer to autumn. The meandering flow was stably confined to the southern part because of the dominant southward eddy momentum fluxes, which were caused by the northwest-southeast inclinations of meandering ridge-axes. Owing to such seasonal change in the lateral transports of momentum and heat, the meandering TWC (or CIC) flow pattern was maintained as a "dynamic equilibrium state".

Key words : Cooling induced current (CIC), Tsushima Warm Current (TWC), meandering pattern, standing Rossby wave, lateral transports of momentum and heat

Introduction

The Japan Sea is a marginal sea in the western North Pacific, connected to adjacent seas through three shallow straits less than 150 m deep, i.e., the Tsushima/Korea, Tsugaru and Soya Straits. The mean depth of the Japan Sea is about 1,500 m, so deep water is completely separated from the other seas. The cold (<1°C) nearly homogeneous water in the deep part of the basin is called the Japan Sea Proper Water (JSPW). The Tsushima Warm Current (TWC) dominates the upper layer flow from the Tsushima/Korea Strait and carries warm water northward to about 40°N (Fig. 1(a)). A polar front with a stable thermal contrast forms along this latitude throughout the year (e.g., Isoda et al., 1991 ; Isoda et al., 1992a ; Isobe and Isoda, 1997). Outflowing water through the Tsugaru and Soya Straits comprises inflowing water of the TWC and upwelled cold water from the intermediate waters in the Japan Sea, which can compose up to several tens of percent of the outflow (Nakajima et al., 2008 ; Ida et al., 2016 ; Kuma et al., 2014 ; Iida et al., 2018). This suggests that some of inflowing water sinks into the middle and deeper layers in the Japan Sea. It seems that outflowing water does not preserve at least the properties of inflowing water even though the volume transport balance through the straits can be taken.

The primary driving force of the TWC system is the sea level (pressure) difference between the East China Sea and sea areas east of the Tsugaru or Soya Straits, i.e., the inflow-outflow dynamic process. Minato and Kimura (1980) first proposed, based on Stommel's theory (Stommel, 1948), that the sea surface height difference between the north and south straits might be caused by wind-driven circulation in the North Pacific, and this difference might drive the inflow of open ocean water into the Japan Sea. Many studies (e.g., Yoon, 1982a, b ; Kawabe, 1982 ; Ohshima, 1994 ; Holloway et al., 1995 ; Kim and Yoon, 1996 ; Nof, 2000 ; Seung, 2003) applied this basic idea to numerical or analytical models with the inflow-outflow forcing through the straits. The success of these external forcing models showed that two types of boundary flow were controlled by the planetary-β and topographic-β effects. One is the Western Boundary Current (WBC) along the Korean peninsula, and the other is the coastal boundary currents along the shelf off the Japanese islands. In addition, a local sea level difference across the Tsugaru or Soya Strait is given after the partial reflection phenomena due to the genesis of gravitational waves over the

[1] *Graduate School of Fisheries Sciences, Hokkaido University*
(北海道大学大学院水産科学研究院)
[2] *Laboratory of Marine Environmental Science, Faculty of Fisheries Sciences, Hokkaido University*
(北海道大学大学院水産科学研究院海洋環境学分野)

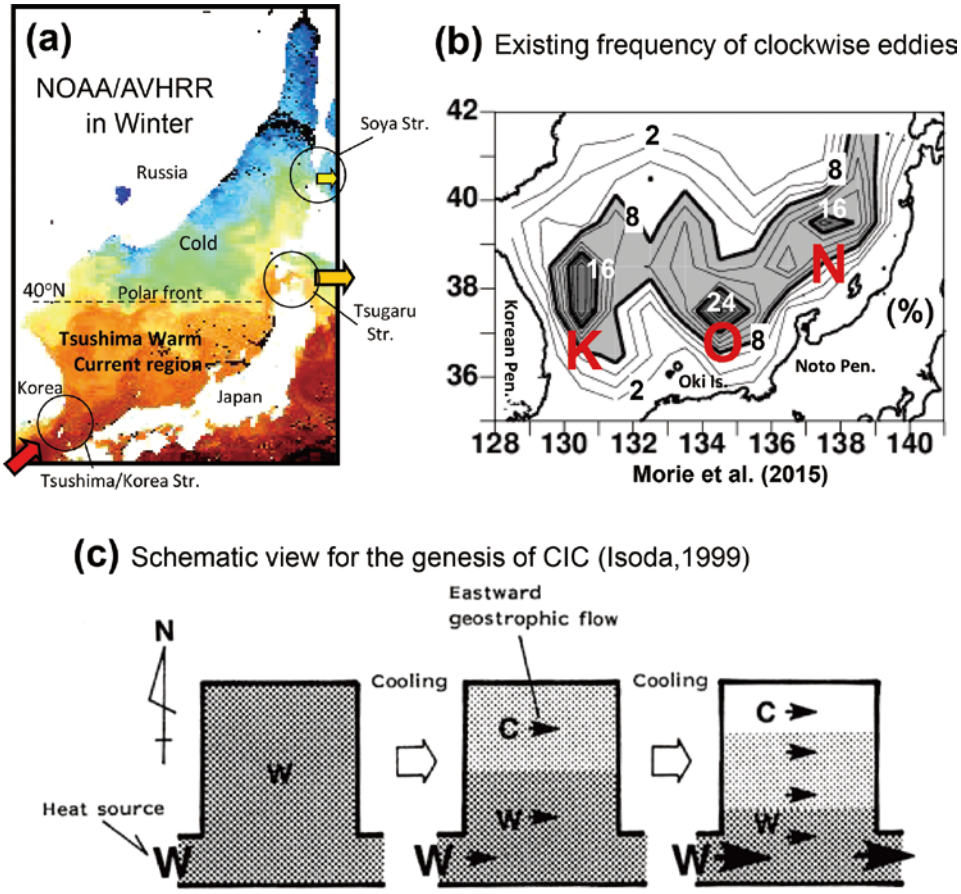

Fig. 1. (a) Snapshot satellite infrared image around the Japan Sea in winter, retrieved by NOAA/AVHRR (http://odyssey.fish.hokudai.ac.jp/AVHRR/). The tremendous contrast of the polar front between southern warm and northern cold waters is clear. (b) Spatial distribution of the existence frequency for warm eddies, made by the long-term statistical analysis of the satellite altimeter data (Fig. 9(d) of Morie et al., 2016). Each symbol K, O and N with higher value means the location of "east of Korean peninsula", "north of Oki islands", and "east of Noto peninsula", respectively. (c) Schematic view for genesis of the CIC system in the upper ocean of the Japan Sea (Fig. 2(b) of Isoda, 1999).

sill-topography in a nonlinear system (Iino et al., 2009 ; Ida et al., 2016). In other words, part of the inflow energy cannot pass through the strait and accumulates at the upstream side causing a rise in sea level, i.e., the occurrence of "form drag" caused by topographically forced waves. Therefore, the disturbance on this rise at the downstream straits can be immediately communicated to the sea level variation at the upstream Tsushima/Korea Strait by gravitational waves with fast propagation speed (Kida et al., 2016 ; Han et al., 2018).

The flow pattern outside the boundary flows, i.e., the TWC in the interior region, indicates complicated meandering, accompanied with several synoptic warm/cold eddies (e.g., Isoda and Nishihara, 1992 ; Isoda et al., 1992b ; Isoda and Saitoh, 1993 ; Isoda, 1994a ; Isoda, 1996 ; Isoda, 2004). In general, it is difficult to specify this interior flow as a prominent single flow path. A typical pattern was described by Morie et al. (2015), who found a quasi-stationary meandering flow pattern with a wave number of three. Specifically, warm eddies remain relatively stable around K, O and N areas shown in Fig. 1(b). Further, Isoda (1999) emphasized that net heat loss through the sea surface is responsible for the maintenance of the TWC in the interior region (eastward geostrophic flow) caused by the meridional thermal/density gradient. This scenario was derived from the following consideration : if the Japan Sea is supplied with heat not only from the lateral advection of TWC but also at the sea surface, the water temperature in the whole area will increase, and the polar front will not form. Without worrying about that, excess cooling through the sea surface in winter has been confirmed by heat budget analyses (e.g., Kato and Asai, 1983 ; Iwasaka and Hanawa, 1990 ; Hirose et al., 1996 ; Na et al., 1999). Isoda (1999) called this flow process a "cooling induced current" (CIC) to distinguish it from the physical process of inflow-outflow forcing.

Reconsidering the equilibrium heat balance on the whole Japan Sea with renewed interest, Isoda (2003) revealed that the above excess cooling occurs under two conditions : 1) a closed deep basin, and 2) lateral heat transport to the southern upper layer. This is realized by heat transport through deep waters (JSPW), because the downward heat supply from the

TWC to deep water must be balanced by heat loss from the sea surface. Especially, the northern deep waters continuously transfer heat to upper waters, and hence both waters are easily mixed vertically. Such a heat condition would produce a significant thermal front at the northern boundary of the TWC, i.e., genesis of the polar front. Then, the northward heat transport of the TWC in the upper layer is regarded to balance the heat loss from the sea surface. Generally speaking, excess cooling through the sea surface in winter (net heat loss) naturally occurs owing to continuous warming of deeper water in a closed basin. In this sense, the JSPW region is always in an unsteady state, as has been shown using geochemical data (e.g., Gamo et al., 2001 ; Kang et al., 2003 ; Kim et al., 2004 ; Kumamoto et al., 2008 ; Gamo, 2014).

Under the net heat loss through the sea surface in the Japan Sea, Isoda (1999) described the formation of the CIC as follows (see Fig. 1(c)). At first, water in the northern area gradually cools in winter, because it is far from the heat source in the southwestern strait (Tsushima/Korea Strait) where the water mass cannot cool due to the large heat supply from the Kuroshio in the North Pacific. Next, in proportion to this meridional thermal gradient, the eastward geostrophic CIC will be generated on the planetary-β plane. As a consequence, warm waters of the East China Sea will be brought into the Japan Sea through the Tsushima/Korea Strait, resulting from the propagations of wave-like disturbances, e.g., Rossby and Kelvin waves. Thus, the CIC acts on the interior forcing in contrast with the external forcing of the inflow-outflow process. Isoda (2011) tried to predict the future of the TWC assuming that the CIC process would gradually weaken due to the recent global warming and then cautioned that the JSPW in an unsteady state could keep warming regardless of global warming. However, the inflow from the East China Sea must be predicated on the sea surface height difference in the North Pacific. We should regard the dynamical state of the TWC system as a modified inflow-outflow process due to the CIC. In this sense, sea surface cooling may be the secondary driving force of the TWC system to justify the steady state for the heat balance.

Isoda (1999, 2003) presented physical hypotheses of the CIC as thought experiments using an idealized box model without dynamical consideration using a realistic numerical model. Several studies have developed numerical models under actual conditions including seasonal variations of wind stress and heat flux (e.g., Yoshikawa et al., 1999 ; Kim and Yoon, 1999 ; Kim and Seung, 1999 ; Tsujino et al., 2008). These models seemed to underestimate the vertical heat advection because the heat flux was indirectly given by assimilating observed temperature into the model surface gird. Therefore, all solutions produced branching currents along the boundaries, but the significant meandering flow of the TWC could not be reproduced. Using a semi-analytical model with an idealized buoyancy forcing (Spall, 2002), Seung and Kim (2011) first suggested that the effective local buoyancy forcing is essential for the formation of seasonally varying eastern and western boundary currents. However, the interior meandering flow was not formed yet, presumably because of oversimplification in their analytical model.

We believe that when the sea surface heat flux (buoyancy) is explicitly forced, the CIC will appear as the characteristic flow pattern that satisfies the heat balance in the Japan Sea. In the present study, we investigated the dynamics of the CIC accompanied with the seasonal variations using a multi-layered numerical model in which the essential conditions allowed for two heat fluxes : 1) excess sea surface cooling at the annual mean state and 2) a continuous lateral heat supply from the southwestern entrance. There was no momentum supplied from the wind stress and no explicit external forcing of the inflow-outflow process. Such systems have emerged from efforts to include entrainment and thermodynamics between the surface and middle layers. Their advantage is dynamical simplicity, which allows only the CIC process at work to be readily diagnosed. As a further simplification, the major limitation in our model is that since the deep ocean is assumed inert, any effects due to bottom or shelf topographies are explicitly excluded.

Model description

To interpret the dynamics of the CIC process, a rectangular ocean (1,000 km × 800 km) with flat bottom topography (500 m depth), connecting two artificial channels (200 km long × 100 km wide) with open boundaries at 200 m depth was adopted in a model (Fig. 2(a)). The actual bottom depth is much deeper in the Japan Sea, but 500 m roughly corresponds to the depth of intermediate layer waters characterized by a salinity maximum (e.g., Matsuoka et al., 2019), and hence the bottom friction can be set to zero. The southwestern channel corresponds to the Tsushima/Korean Strait and the northeastern one to the Tsugaru or Soya Strait. The ocean model used was the multi-layered Princeton Ocean Model (POM, Blumberg and Mellor, 1987) on the planetary-β plane. The parameter f_0 was evaluated at 33°N so that $f_0 = 7.0 \times 10^{-5}\,\mathrm{s}^{-1}$ and $\beta = 1.8 \times 10^{-11}\,\mathrm{m}^{-1}\,\mathrm{s}^{-1}$. We used Cartesian coordinates where the direction of the x-axis was 20° from east to north. The density field was a function of only water temperature (salinity fixed at 34.0 psu).

The model was driven by net heat flux through the sea surface, for simplicity, which was assumed to be spatially uniform over the entire model domain. Using long-term observation data, Hirose et al. (1996) assessed that the annual averaged net heat flux over the entire Japan Sea was negative and ranged from -25 to $-85\ \mathrm{W\,m^{-2}}$. Based on their study, we selected an annual mean cooling flux of $a = -70\ \mathrm{W\,m^{-2}}$ and a seasonal amplitude with flux of $b = 214.5\ \mathrm{W\,m^{-2}}$ varying sinusoidally over time. So, the net heat flux

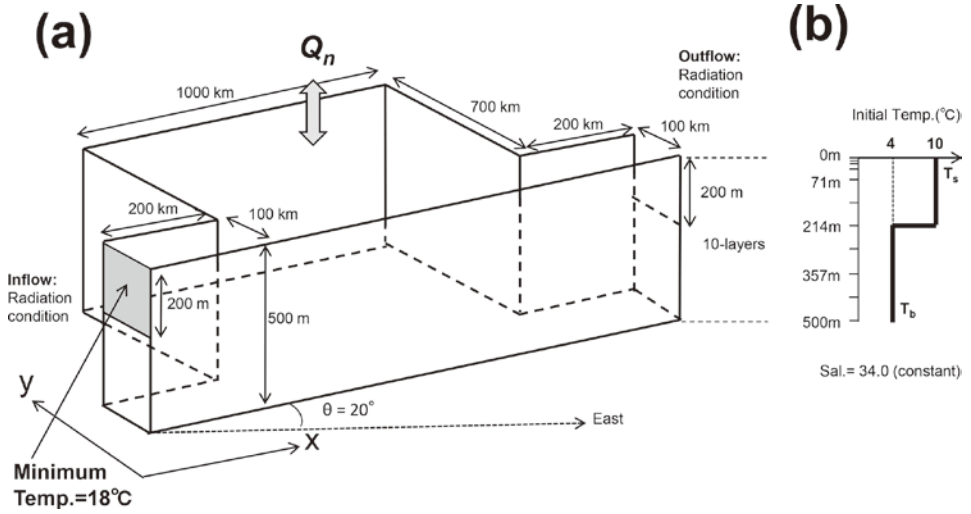

Fig. 2. (a) Multi-layered rectangular ocean model (POM) on the planetary-β plane, driven by the seasonal change in sea surface heat flux with excess cooling (Q_n), is used to investigate the dynamics of the CIC in the Japan Sea. (b) Vertical profile of initial water temperature in this model.

Q_n was composed of mean and time-dependent parts as follows :

$$Q_n = b \cdot \sin\left(\frac{2\pi}{P}t + \frac{3\pi}{2}\right) + a \qquad (1)$$

where P is the period of a one-year cycle (360 days). In this model, the heating maximum of 145 W m^{-2} occurred from June to July, and the cooling maximum of -285 W m^{-2} occurred from December to January. In another experiment forced by the annual constant cooling, we set $b = 0$.

As mentioned in the introduction, there is a unique lateral heat source west of the Tsushima/Korea Strait at the open boundary of the southwestern channel. In our CIC model with the radiation condition without velocity forcing at the open boundaries, the inflow-outflow through the boundaries could be naturally generated by the propagations of interior disturbances. To represent such a heat flux inflow across the section of southwestern boundary ($x = 0$), 18ºC seawater was advected when $u\partial T(y,z)/\partial x < 0$ (u is velocity in the x direction) mainly during the cooling season, but the water temperature increased according to the boundary condition of $\partial T(y,z)/\partial x = 0$ when $u\partial T(y,z)/\partial x > 0$ during the heating season. During the cooling season, the instantaneous vertical mixing resulting from the convection adjustment mechanism was used to avoid unstable density stratification.

Grid spacing was 5 km × 5 km, which is sufficient to reasonably resolve an internal radius deformation of about 30 km in the TWC region of the model. There were 10 vertical layers, and the thickness of each layer from top to bottom was 9 m × 2, 18 m, 35.5 m, and 71.5 m × 6. The time step was set at 450 s. The horizontal eddy viscosity and diffusivity coefficients were set at $A_h = 10^3$ m^2 s^{-1} and $K_h = 5 \times 10^2$ m^2 s^{-1}, respectively. The vertical eddy viscosity coefficient and diffusivity coefficients were both set at $A_v = K_v = 10^{-4}$ m^2 s^{-1}.

Initially, the horizontal gradient of water temperature was zero, i.e., the upper layer (0～214 m) was filled with 10°C water and the lower layer (214～500 m) was filled with 4°C water (Fig. 2(b)). Time integration continued until the end of the 25th year when the model ocean reached a seasonal variable equilibrium. The results from the 25th year are discussed in the following sections. In the experiment for annual constant cooling, time integration over 45 years was needed to reach a steady state.

Initial response and response time of the cooling induced current

First, we examined the initial response of the model ocean (Fig. 3). After 10 months, the surface temperature T_s at the northern part rapidly decreased because of excess cooling in winter and warmer (less dense) water was confined to the southern coast. This meridional thermal/density gradient surely generated the eastward geostrophic flow path, which connected the inflow at the southwestern channel with the outflow at the northeastern channel (not shown). In our CIC model with a flat bottom, the internal Kelvin waves propagating from the heat source at the inflow channel contributed to determining the flow path along the coast. As time elapsed from 22 to 58 months, warmer water gradually moved offshore or northwestward from the southern coast due to the propagation of planetary Rossby waves, while the northern temperature continued to decrease. Although the meandering with a wave number of four was developing around 58 months (during the 5th year), its wave number decreased and was finally close to three at a steady state after the 25th year (see Fig. 4(a)), probably according to the increase of inflow volume transport.

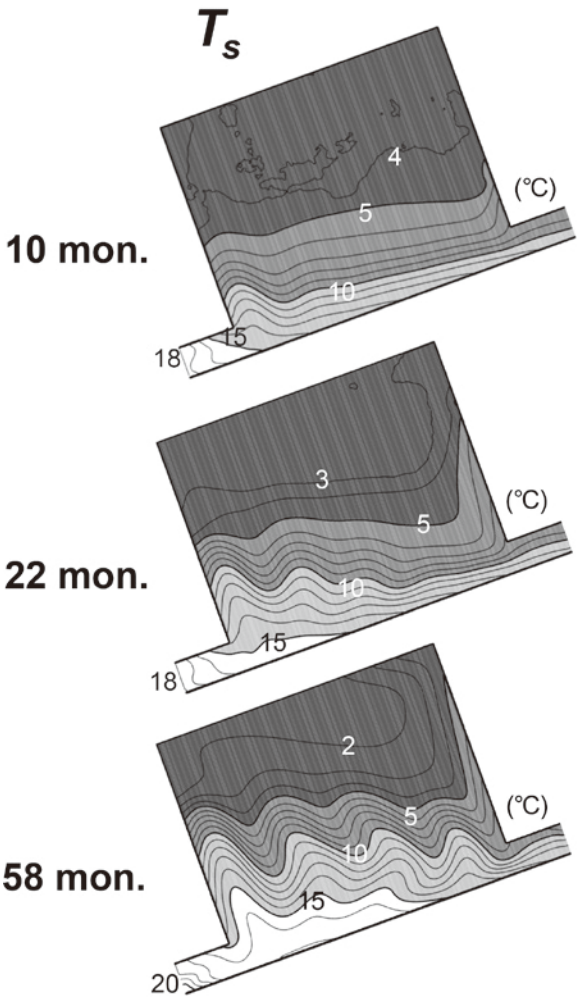

Fig. 3. Surface temperature T_s fields at 10, 22 and 58 months (0.83, 1.83 and 4.83 years) after the start of seasonal sea surface heat flux Q_n forcing.

Some characteristics of such an initial response could be found in previous studies of interannual variations of the TWC. Using the long-term data of sea surface temperature in winter and coastal sea level, Isoda (1994b) suggested that water from the East China Sea is brought into the Japan Sea by cooling strengthened TWC, remarkably on a decadal time scale. Further, there are reports of interdecadal variations of 1) hydrographic properties across the vertical section of the TWC (Isoda and Korematsu, 1995), 2) surface mixed layer water of the TWC region (Isoda and Kim, 1998), and 3) inflow pattern around the Tsushima/Korea Strait (Isoda and Tanaka, 1999). These three studies showed that relatively cold, low-salinity waters appeared in the TWC region in cold winters during the 1980's and were closely connected with an intensified inflow from the East China Sea.

Further, to extract such a response of the CIC component from satellite Sea Surface Height Anomaly (SSHA) data, Takamasu et al. (2019) carried out harmonic analysis of the SSHA for a 8-year period with respect to similarities in the interannual variation of the Asian Monsoon Index (MOI). Their results confirm that the northeastward flow off the shelf edge along the Japanese islands intensified only in the coldest years, which is suggested by the maximum MOI. This intensified CIC gradually migrates offshore for two years, and then connects to the inflow in the Tsushima/Korea Strait via the east coast of Korean peninsula with a time lag of about three years. Thus, the actual response time scale of the CIC and the model response was several years or more, which is longer than seasonal variation with a one-year cycle.

Annual mean state of the cooling induced current

Annual mean flow field and volume transport

In the statistically steady state in the 25th year (Fig. 4), the annual mean distribution of surface flow essentially represented the inflow-outflow circulation on the planetary-β plane, but what was remarkable was the meandering CIC, which widely extended to the southern part of the model ocean. The northward WBC formed along the western coast, and its northern end was nearly confined by the latitude of the outflow channel (Fig. 4(c)). However, the WBC had an eastward geostrophic component in proportion to the meridional broad pressure gradient, depending on surface temperature or sea surface height fields (Figs. 4(a), (e)). Therefore, the northward flow speed of the WBC gradually weakened, and the eastward flow separated from the WBC in the southern interior region. From satellite-tracked drifter observations in the Japan Sea, Lee et al. (2000) found that drifters frequently left the WBC region and moved to the east.

We identified the polar front as a relative clear thermal contrast, but the eastward flow accompanied by this front was not so strong (Figs. 4(a), (c)). The northern sea area was occupied by uniform cold waters less than 5°C (Fig. 4(a)) and had the lowest sea level (less than −40 cm) in the whole model domain, which is much lower than at the outflow channel (nearly −20 cm) (Fig. 4(e)). Our CIC model eventually produced the inflow-outflow circulation. However, the extremely low sea level north of the polar front was never reproduced by the inflow-outflow forcing alone, but resulted from the CIC model.

Although the net eastward volume transport (*net-Ve* = *Ve* + *Vw*) had a local maximum in September, its annual range was about 0.3 Sv (Fig. 5(d)), which is much smaller than the observed one (Takikawa and Yoon, 2005). On the other hand, the annual mean volume transport of *net-Ve* through both channels was about 2.15 Sv (Fig. 5(d)), which is close to the typical order of the TWC at the Tsushima/Korea Strait. It is interesting that the annual mean eastward component ($Ve > 0$) increased drastically across the central section ② in comparison with those at channels ① and ③ (Fig. 5(b)). It increased by 1.35 Sv to 3.50 Sv. This increase was supplied by cold waters (< 3°C) from the lower layer (see

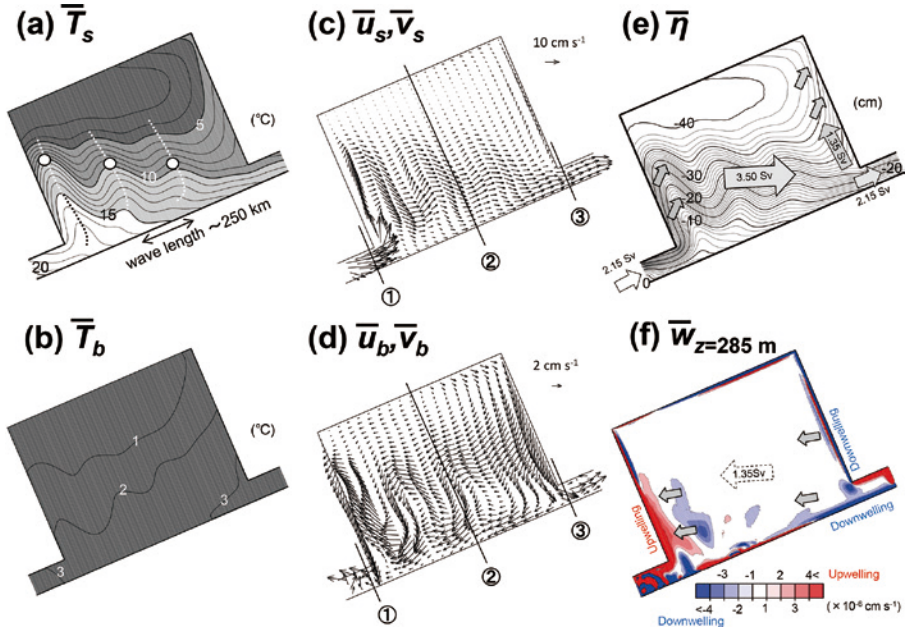

Fig. 4. Annual mean horizontal distributions of the (a) surface temperature $\overline{T_s}$, (b) bottom temperature $\overline{T_b}$, (c) surface current vectors $\overline{u_s}\cdot\overline{v_s}$, (d) bottom current vectors $\overline{u_b}\cdot\overline{v_b}$, (e) sea surface height $\overline{\eta}$, and (f) vertical velocity at 285 m depth $\overline{W_{z=285m}}$, respectively. Three open circles with dotted lines in (a) denote the ridges of meandering flow. These ridge-axes tend to be inclined from northwest to southeast. The volume transports discussed by using Fig. 5 are calculated across three lines in (c) and (d), named by symbols of ① (inflow channel), ② (central section) and ③ (outflow channel).

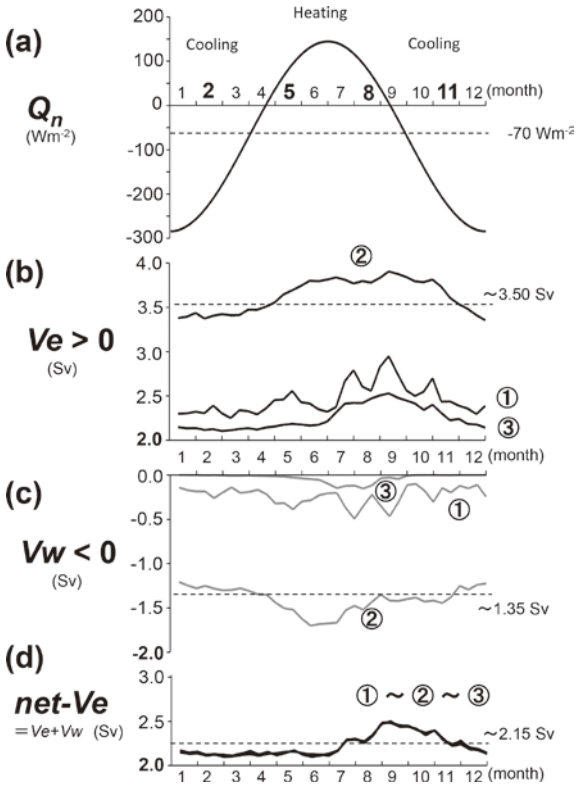

Fig. 5. (a) Sinusoidal function of forced sea surface heat flux Qn with a one-year cycle. The seasonal change in reproduced volume transports for the (b) eastward component ($Ve>0$), (c) westward component ($Vw<0$), and (d) net eastward component ($net\text{-}Ve=Ve+Vw$) across three lines (①, ② and ③), shown in Figs. 4(c) and (d).

Fig. 4(b)) with a reverse transport of $Vw=-1.35$ Sv (② of Fig. 5(c)) through upwelling along the WBC (red area in Fig. 4(f)). Continuity requires downwelling along the eastern coast (blue area in Fig. 4(f)). These flows are schematically shown by arrows in Figs. 4(e) and (f). This latitudinal vertical circulation (recirculation process within the Japan Sea) and the extremely low sea level at the northwestern part are unique characteristics of the CIC model.

Yoshikawa et al. (1999) studied overall features of basin-scale model circulation of the intermediate water using the annual mean Lagrangian velocities on the 32 σ_1 surface (nearly 27.3 σ_θ surface). Lagrangian velocity field shows that southwestward transport of the intermediate water takes two major routes : along the continent in winter and along the Japanese coast in summer. Matsuoka et al. (2019) examined hydrographic data in the Japan Sea to understand the transport path of High Salinity Intermediate Water (HSIW) with a density greater than 27.3 σ_θ. The spatial distribution of the acceleration potential on the 27.33 σ_θ surface suggests that HSIW was transported southwestward from the subarctic area north of the polar front. Mori et al. (2006) also investigated hydrographic data along two observation lines west of the Tsugaru Strait and showed that HSIW tended to appear more prominently in autumn than in spring. This seasonality of HSIW appearance is qualitatively consistent with our model result. As seen in ② of Fig. 5(c), the westward bottom flow ($Vw<0$) across the central section has a local maximum in June between spring and autumn. Thus, this intermediate flow with HSIW must be evidence for the west-

ward bottom flow (Fig. 4(d)) below the eastward TWC (Fig. 4(c)).

Meandering pattern

The lateral wave number of the reproduced meandering flow was three, and its wavelength was about 250 km. This is similar to the quasi-stationary flow pattern of the TWC, i.e., typical three major warm regions shown in Fig. 1(b). There are two possible formation mechanisms for such a meandering : an instability wave and a standing Rossby wave. We confirmed that the former possibility was low (see Appendix A for details), and hence the latter possibility will be proposed in this study.

For a density-driven solution in our CIC model, there was upwelling/downwelling along the western/eastern boundary and westward flow at the bottom of the upper layer, both associated with the thermal-wind circulation and existing only on the planetary-β plane. Upwelling of cold water along the western boundary considerably weakened the warmer WBC, so a broad eastward flow originating from the WBC was generated in the whole TWC region. In such a physical situation, the standing Rossby wave is thought to have formed by the westward propagation speed of the baroclinic Rossby waves balancing a broad eastward flow speed.

Here, the analytic theory of a standing Rossby wave using a reduced gravity model of Morie et al. (2015) extends to that of the two-layered model. When the meridional averaged surface velocity of eastward meandering flow is given by U, the dispersion relations of the surface-trapped ($|A/B|>1$) and bottom-trapped ($|A/B|<1$) disturbances are given as the frequencies $\sigma_+(k)$ and $\sigma_-(k)$ (see Appendix B for their derivations). Any constants of A and B are the upper and lower disturbance amplitudes, respectively. Using several parameters of our model result, the obtained dispersion curves and the amplitude ratios of A/B are shown in Fig. 6(a) when U = 2.2 cm s^{-1} and, for comparison, in Fig. 6(b) when U = 0.0 cm s^{-1}. It is understood that a positive U changes the barotropic Rossby wave ($U = 0$ and $A/B = 1$) of $\sigma_-(k)$ to the bottom-trapped wave in all wave numbers and the baroclinic Rossby wave ($U = 0$ and $A/B = -1.5$) of $\sigma_+(k)$ to the surface-tapped or bottom-trapped wave depending on the wave number.

Since each curve of $\sigma_+(k)$ and $\sigma_-(k)$ in Fig. 6(a) is independent, i.e., non-resonant state, we can reaffirm that the meandering was not a baroclinic instability wave. As will be shown later, it seems that even under the seasonal change in heat flux, the meandering state with wave number of three remained almost unchanged in all seasons. On the dispersion relation, this state corresponds to the standing Rossby wave with zero frequency. It is denoted by a small open cir-

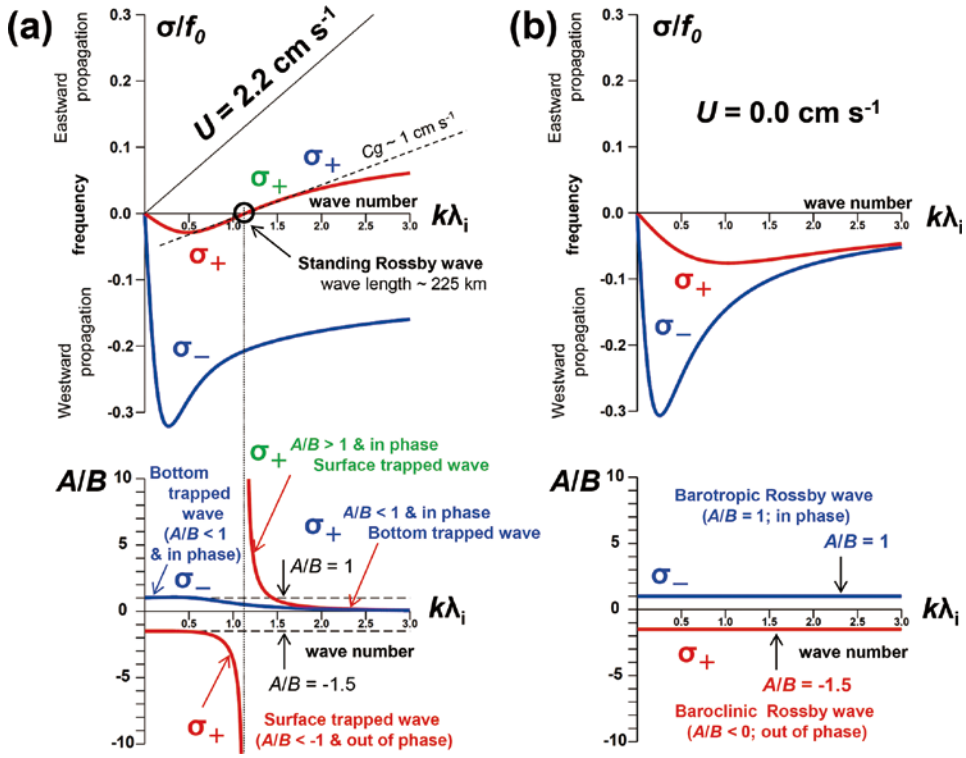

Fig. 6. (a) Upper panel is the dispersion curves of σ_+ (surface-trapped wave with $|A/B|>1$) and σ_- (bottom-trapped wave with $|A/B|<1$) in eqs.(A12)~(A16) using the parameters of model result. Lower panel is the same as upper panel except the amplitude ratio of surface-trapped (A) to bottom-trapped (B) disturbances. If $A/B > 0$ ($A/B < 0$), the upper and lower disturbances are in phase (out of phase). (b) is the same as (a) except for U = 0.0 cm s^{-1}, and is drawn to theoretically understand the effect of U on the dispersion relation.

cle in the upper panel of Fig. 6(a), where a curve $\sigma_+(k)$ of the surface-trapped wave intersects the axis of wave number. That is, the phase speed is zero as $\sigma_+(k) = 0$, and the wavelength is about 225 km. Note that this standing Rossby wave has a non-zero group velocity of $Cg \sim 1.0$ cm s$^{-1} > 0$ (inclined broken line), which is about half of the eastward mean flow speed $U = 2.2$ cm s$^{-1} > 0$ (inclined solid line). This positive group velocity of surface disturbance implies that the kinetic energy of the standing Rossby wave is always transported downstream. In addition, the amplitude ratio A/B of standing Rossby wave is infinite, i.e., solution for surface disturbance only with $B \sim 0$. This implies that the TWC in the standing Rossby wave state becomes harder to feel the bottom topography. If so, the reduced gravity model of Morie et al. (2015) may still be a useful theory to discuss the TWC as a standing Rossby wave.

As for the interannual time-varying flow pattern, Morie et al. (2015) reported that abrupt developments and declines of the meandering TWC were observed three or four times during 1993-2011. Using a reduced gravity model forced by temporal change in eastward flow speed, Morie et al. (2015) inferred that such successive increases in amplitude occur according to a certain value of eastward flow speed, and asymmetrical response in periods of increasing and decreasing eastward flow appears due to the different dispersive properties of Rossby waves. If this speculation is correct, it will be very difficult to predict whether meandering will develop or not. More detailed discussion for such interannual response, however, is beyond the scope of the present study and is a future issue.

Difference from the experiment without seasonal change in surface heat flux

On the mechanism for the genesis of the CIC proposed by Isoda (1999), the seasonal change in surface heat flux is not always necessary. Therefore, the model result forced by the annual constant negative heat flux, i.e., constant sea surface cooling, can produce the CIC (Fig. 7(a)). However, its flow structure differed from that of the annual mean state with seasonal change in heat flux (Figs. 4(a), (c)). To enhance the difference from the results of annual mean state with seasonal heat flux, the horizontal distributions of anomalies for $\Delta T_s = T_s - \overline{T_s}$ and $\Delta u_s = u_s - \overline{u_s} \cdot \Delta v_s = v_s - \overline{v_s}$ are shown in Fig. 7(b). In the model without seasonal heat flux (Fig. 7(a)), surface eastward density current widely spread to the northern end, and the meandering was not clear. In a difference from the model with seasonal heat flux (Fig. 7(b)), the water temperature increased in most areas except in the north-

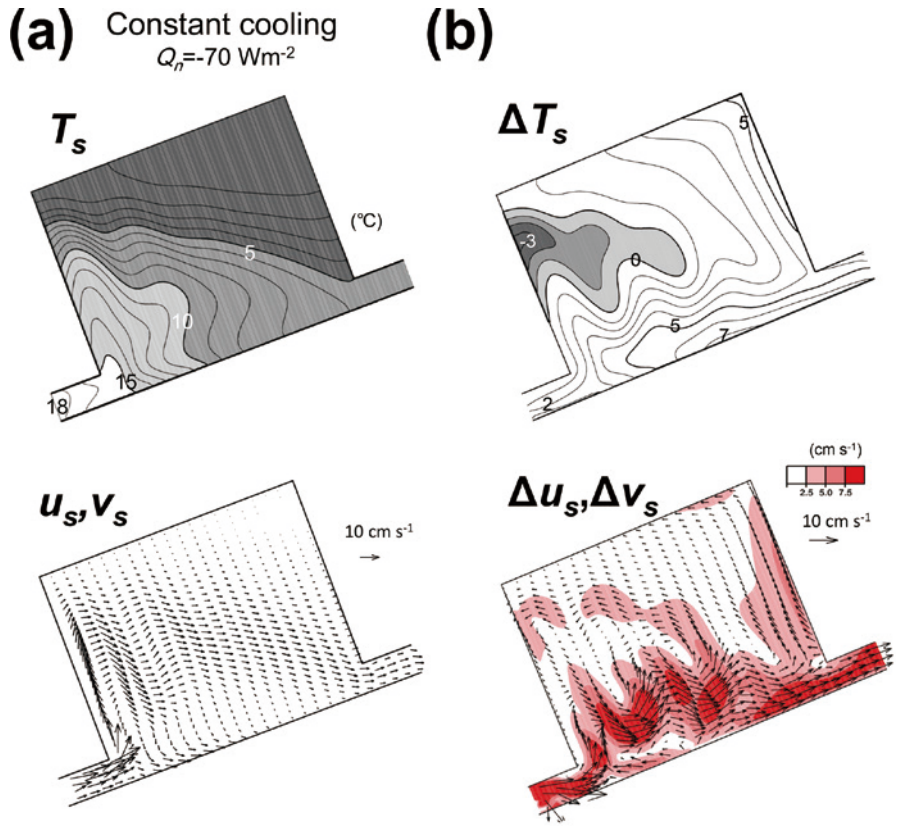

Fig. 7. (a) Steady state after 45 years for the surface temperature field T_s and the surface current field $u_s \cdot v_s$ in the model forced by annual constant cooling. (b) Horizontal distributions of their anomalies from the annual mean surface temperature $\overline{T_s}$ in Fig. 4(a) and the annual mean surface current $\overline{u_s} \cdot \overline{v_s}$ in Fig. 4(c), i.e., $\Delta T_s = T_s - \overline{T_s}$ and $\Delta u_s = u_s - \overline{u_s} \cdot \Delta v_s = v_s - \overline{v_s}$ fields, respectively.

western area (this area had a negative ΔT_s value), and the eastward flow confined by the southern region disappeared (this is indicated by locally intensified eastward flow of Δu_s, Δv_s). Yoon (1982a) carried out a similar numerical experiment under the annual mean atmospheric conditions and also pointed out that a sharp thermal front corresponding to the polar front did not form.

Our interpretation of the result in Fig. 7(a) is as follows. To balance the annual constant heat loss from the sea surface, there must be lateral heat transport. Therefore, as a necessity, warmer water is advected as northward as possible along the western boundary and is steadily supplied to the whole area by an eastward flow spreading in the meridional direction. Conversely, in the model with seasonal heat flux, the loose restriction satisfying net heat balance within a one-year cycle was responsible for the formation of a significantly meandering CIC. That is, owing to the seasonal change in heat transport, the meandering flow pattern was maintained as the annual equilibrium state, so in the present study we call this the "dynamic equilibrium state" of the CIC.

Seasonal variations in the cooling induced current

Sea surface temperature

The temperature field showed seasonal variation (Fig. 8(a)), i.e., a basin-scale warm in August during the heating season and cold in February during the cooling season. The northern end of the warm region (the polar front) exited throughout the year. Its position was almost stationary, but its intensity strengthened in summer (August) and weakened in winter (February). As mentioned earlier, the meandering with a wave number of three remained in nearly the same location all seasons.

The most remarkable seasonal variation of temperature occurred along the northeastern boundary, suggesting a downwelling (Fig. 4(f)), which corresponds to the western area of Hokkaido located north of Tsugaru Strait. Around this area from February to May, the coldest water was less than 5°C, and the warmer TWC disappeared. After the start of heating in May, the coastal trapped thermal flow intruded slowly northward from August to November. Such a pattern variation is consistent with that of observational study by Higaki et al. (2008), who reported the seasonal occurrence of the TWC based on the mode-water analysis using hydrographic data off

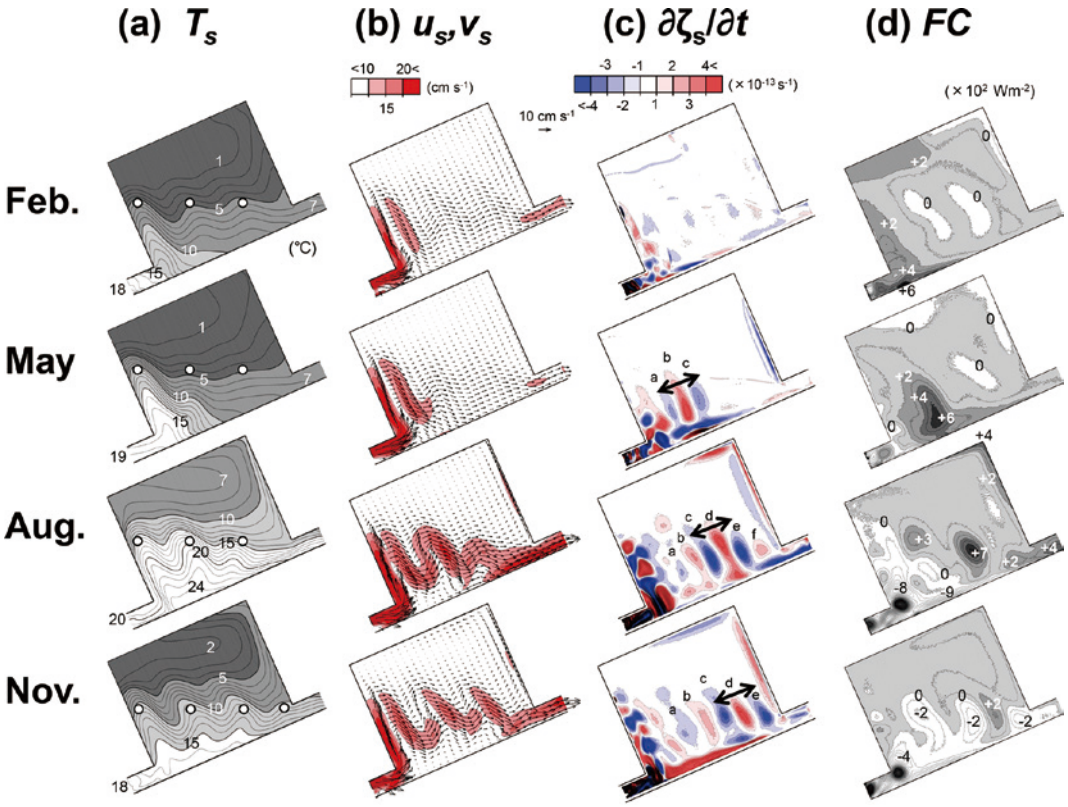

Fig. 8. Seasonal change in the horizontal distributions of the (a) surface temperature T_s, (b) surface current vector $u_s \cdot v_s$, (c) temporal variation of relative vorticity at the sea surface $\partial\varsigma_s / \partial t$, and (d) lateral heat transport FC, shown by successive four months of February, May, August and November. Open circles in (a) denote three ridges of meandering flow. Strong current speed (> 10 cm s^{-1}) in (b) is enhanced by red color. The locations of positive (red color) and negative (blue color) $\partial\varsigma_s / \partial t$ in (c) are shown using letters "a" to "f". The area with positive higher transport in (d) is highlighted by the darker gray scale, while white area denotes a negative transport.

the west coast of Hokkaido (not shown).

Surface flow pattern

Figure 8(b) shows the seasonal change in surface velocity field $u_s \cdot v_s$ in the same months of T_s shown in Fig. 8(a). The surface flow showed an evident meandering, which weakened in February and strengthened in August. To examine the seasonal evolution and decay for the meandering, temporal change in relative vorticity (ς_s) at the sea surface, i.e., $\partial\varsigma_s / \partial t$, was calculated each month (Fig. 8(c)). When the meandering intensified from May to November, the east–west locations of positive and negative $\partial\varsigma_s / \partial t$ areas are shown using letters "a" to "f". In May, striped pattern of $\partial\varsigma_s / \partial t$ from "a" to "c" first appeared at the western/upstream side. After that, the similar pattern from "d" to "f" gradually intensified in turn further to the eastern/downstream side. Although the locations of "a" to "f" remained almost unchanged, the intensified pattern denoted by an arrow slowly moved eastward/downstream with a propagation speed of 1.0 ～1.6 cm s^{-1} = (300～500 km)/360 days. This implies that the disturbance accompanied by meandering had a nearly zero phase velocity and a positive group velocity. Such properties are consistent with the dispersive characteristics of standing Rossby wave (Fig. 6 in this paper) and are similar to the seasonal change in relative vorticity estimated from satellite SSHA (Figs. 8(b) and 9 of Asahi et al., 2016).

Annual harmonic component of surface flow

We looked at the anomaly field of velocity from annually averaged values because the seasonal disturbance of a standing Rossby wave affects the genesis of meandering CIC. Using harmonic analysis with a period of 360 days, the horizontal distribution of annual velocity ellipses is shown in Fig. 9(a). Anti-clockwise ellipses (blue) and clockwise ellipses (red) indicate elongate distributions from the northward and southward ridges of meandering, respectively, to the southwest.

Figure 10 displays the anomalies of annual harmonic velocity field every two months from May to November. In May, the inflow at the southwestern channel strengthened, while the outflow at the northeastern channel and the offshore side flow of the meandering weakened. Thereafter, the eastward meandering in whole area gradually intensified, and the meandering became strongest from September to November. Then, the anomaly field in November had the opposite pattern in May. Such a slow intensification of eastward meandering is readily understood by considering a positive group velocity of a standing Rossby wave and can be supported by the flow patterns estimated using coastal sea level data (Fig. 4 of Ishikawa et al., 2007) and satellite SSHA data (Fig. 8(a) of Asahi et al., 2016).

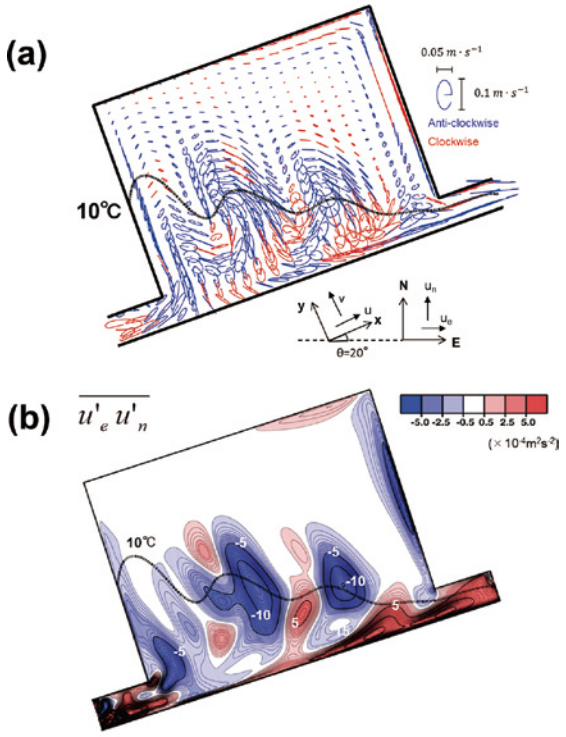

Fig. 9. (a) Horizontal distribution of annual velocity ellipses. Clockwise ellipses are shown in red, and anti-clockwise ellipses are shown in blue. The straight line in each ellipse indicates the phase of 0 day. (b) The horizontal distribution of stress component $\overline{u_e' u_n'}$, averaging one-year by using the velocity ellipse data in (a). A superimposed dotted line in both figures illustrates the surface isotherm of 10°C at the annual mean state.

Seasonal changes in eddy momentum flux and lateral heat transport

North–south transport of eddy momentum flux

Our model results indicate that seasonal disturbance ($u_s' v_s'$) was required to generate the meandering flow pattern ($\overline{u_s} \cdot \overline{v_s}$). Eddy momentum flux accompanied with such a disturbance may be viewed as Reynolds stress with a seasonal time scale. To illustrate the effect of the north–south transport by Reynolds stress on eastward mean flow, Fig. 9(b) shows the horizontal distribution for the stress component $\overline{u_e' u_n'}$ averaged over a one-year period using the velocity ellipse data in Fig. 9(a). The negative flux drawn in blue ($\overline{u_e' u_n'} < 0$) dominated around the interior meandering region. This implies that the eastward flux ($u_e' > 0$) was transported to the south ($u_n' < 0$) or the westward flux ($u_e' < 0$) was transported to the north ($u_n' > 0$), so the eastward mean flow was confined to the southern part and strengthened. The estimated barotropic instability in Appendix A suggests that the index of $N' < 0$ at the southern half area indicates the energy conversion from eddies into the mean flow (see Fig. A1(a)).

Jacobs et al. (1999) analyzed satellite altimeter data for the effect of mesoscale eddy variability in the TWC region and

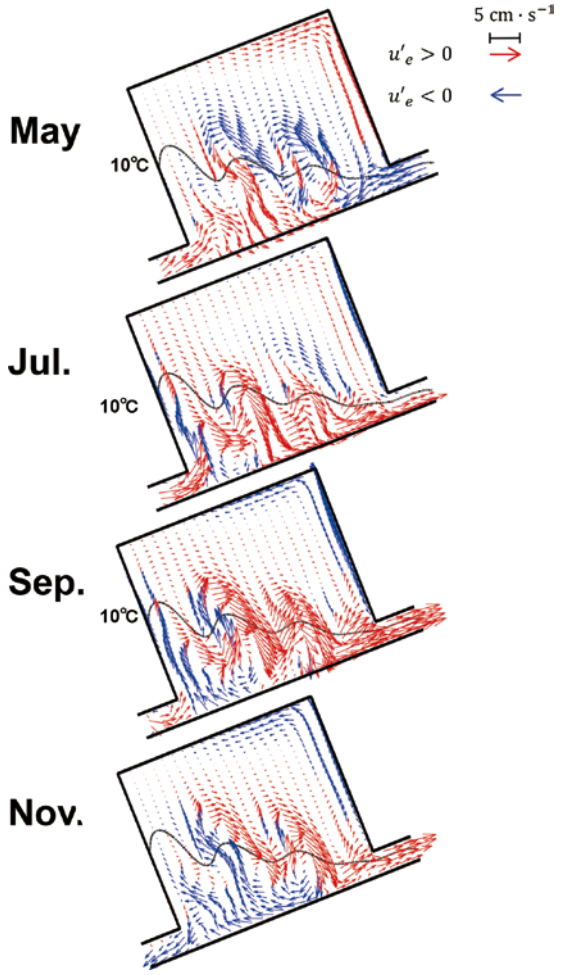

Fig. 10. Anomalies of annual harmonic velocity field every 2 months from May to November, made by using the velocity ellipse data in Fig. 9(a). The velocity vectors with eastward (westward) component are drawn by red (blue) color in order to emphasize the strength sense of eastward meandering.

gave the opposite conclusion from our result, i.e., the momentum flux due to the eddy variability aids in the northward transport. Then, Jacobs et al. (1999) emphasized the importance of mesoscale influence through upper ocean–bottom topographic coupling. Unfortunately, we cannot discuss the cause of both different conclusions, because such coupling effect is explicitly ignored in our model with a flat bottom.

The reason why $\overline{u_e' u_n'} < 0$ occurred in our model is that the direction of ridge-axis of meandering was not just north–south but rather slightly inclines to northwest–southeast, as clearly seen in the meandering pattern itself at the mean state (Figs. 4(a), (c)) and in the temporal disturbances of $\partial \varsigma_s / \partial t$ (Fig. 8(c)). We can expect that this southward transport of the eddy momentum flux will continue to increase indefinitely because these ridge-axes are further inclined by the southern intensified eastward mean flow and, in reverse, its eastward flow is further intensified according to a larger inclined ridge-axis. Such a relationship indicates the positive feedback system, which maintains or strengthens the meandering CIC.

Seasonal transport of lateral heat flux

We consider that the dynamic equilibrium state of flow pattern will be determined by the interaction between southward eddy momentum flux as mentioned in the previous subsection and northward positive-heat transport as examined in this subsection. By subtracting the forced surface heat flux (Q_n) from the temporal change in heat capacity vertically integrated from surface to the model bottom (DH), the lateral heat transport ($FC = DH - Q_n$) is given. Here, DH was calculated by the following equation :

$$DH = \rho_w C_w \Delta \bar{T} / \Delta t \qquad (2)$$

where ρ_w (= 1.025×10^{13} kg m^{-3}) and C_w (= 3.993×10^3 J kg^{-1} ℃$^{-1}$) are the water density and specific heat of seawater, respectively. We selected Δt = 10 days in each month, and $\Delta \bar{T}$ is the temporal change in vertical integrated temperature during the same 10 days.

Figure 8(d) shows the horizontal distributions of lateral heat transport FC in February, May, August and November. These model results can be compared with those of a similar analysis using the observed data, i.e., Fig. 3 of Nakada et al. (2002). The most important result is that a positive heat transport into the model Japan Sea from the southwestern/inflow channel did not occur throughout the year, but only in the late winter. In February during the latter half of cooling season (see Fig.5 (a)), the area with a local maximum positive heat transport appeared along the southern boundary near the inflow channel. In May at the start of surface heating, while the positive heat transport advanced rapidly along the southern coast, its local maximum migrated slightly eastward as forming a large patchiness. Since the meandering intensified during the heating season, this patchiness in August split into several small ones, and were gradually advected offshore and downstream. The observed FC distributions of Nakada et al. (2002) similarly show that several positive patchiness appear along the Japanese islands (Honshu) in spring (April), moves from coastal areas to offshore or north in summer (August). In addition, the model result in August indicated that the negative heat transport (shown in white) appeared mainly around the upwelling region near the WBC. In November during the former half of the cooling season, this negative area widely extended to the meandering TWC region. Interestingly, such negative heat transport also agrees with the observational results in December of Nakada et al. (2002).

Roughly speaking, for the seasonal heat budget in our model result, the positive heat supply from the southwestern channel occurred only in late winter, extended slowly to the TWC region as offshore advection of some meandering patchiness in summer, and then contributed to the heat loss by sea surface cooling in winter. We also suggest that the

whole TWC region is not only cooled in winter, but also eastward advection of upwelled cold waters originating from the WBC region in summer to autumn.

Summary and discussion

In the present study, we succeeded in producing a meandering TWC with an east–west wave number of three using a CIC model forced by seasonal change in sea surface heat flux with excess cooling. The dynamical properties for this meandering were not understood by an instability wave, but could be explained by a standing Rossby wave. Our CIC model's characteristics are as follows 1) latitudinal vertical circulation was caused by upwelling/downwelling along the western/eastern boundary due to the thermal-wind circulation on the planetary-β plane, and 2) the lowest sea level in the northwestern cold region, which was much lower than at the outflow channel. Such a flow pattern never formed in the CIC model forced by annual constant cooling. That is, the meandering TWC had a "dynamic equilibrium state" including seasonal variations of momentum and heat transport. In other words, seasonal disturbance is a necessary condition to generate the meandering flow.

The following scenario was repeated over a one-year cycle. Excess cooling in winter weakened the meandering flow, but strengthened the coastally trapped thermal flow near the heat source of the inflow channel. This thermal flow significantly contributed to the lateral heat supply and the southern intensified eastward flow. On the planetary-β plane, sea surface heating in summer cannot confine the thermal flow near the coastal area, and hence the lateral heat content gradually moved offshore/northward from the coastal area. This offshore heat supply slowly intensified the meandering flow according to an adjustment process of a standing Rossby wave. At this time, the meandering flow could be stably confined to the southern part because of the continuous southward eddy momentum fluxes, which were caused by a northwest–southeast inclination of the meandering ridge-axes. In the next winter, the intensified meandering weakened again.

Our CIC model could reproduce an inflow-outflow system with a reasonable annual mean volume transport, but failed to reproduce the annual range of volume transport. To resolve this failure, the seasonal variable inflow-outflow should be used as the external forcing. It is known that the outflow condition through the Soya Strait showing a clear seasonal variation is very important (Tsujino et al., 2008 ; Kida et al., 2016). Wind-induced flow eliminated in our model also may have affected the advection field of heat transport. For instance, Asahi and Isoda (2017) simulated that the positive curl of wind stress in the northern Japan Sea, where the planetary-β in the lower layer is locally cancelled by the topographic-β, plays an important role mainly in the seasonal change of deeper circulation. If so, the actual bottom topography should be considered. Then, we would be able to discuss the truth of the importance for the eddy momentum flux due to coupling effect between the upper-ocean and topography, suggested by Jacobs et al. (1999). The observed net heat flux through the sea surface, which is actually determined by the interaction between sea and atmosphere, is never spatially uniform (e.g., Hirose et al., 1996). Therefore, the uniform value of heat flux we used has incorrectly overestimated/underestimated the surface cooling in winter at the northern/southern part. Thus, it is difficult to make insight into the dynamics of more realistic complex TWC systems. Nevertheless, our model result is still of interest because the meandering CIC process should be active in the interior flow of TWC region.

Appendix A : Energy transfers for barotropic and baroclinic instabilities

Energy analysis proposed by Masina et al. (1999) was performed to understand the energy generated in the meandering region of our model. Each variable of $V=(u,v)$ (horizontal velocity vector), w (vertical velocity) and ρ (density) can be decomposed into a time mean (annual mean) and a deviation (seasonal variation) forms denoted by overbars and primes, respectively

$$V=\overline{V}+V' \tag{A1}$$
$$w=\overline{w}+w' \tag{A2}$$
$$\rho=\overline{\rho}+\rho' \tag{A3}$$

The equation for eddy kinetic energy $K_e=\frac{\rho_0}{2}\overline{V'V'}$ is given by

$$\frac{\partial Ke}{\partial t}+\left(\overline{V}\cdot\nabla Ke+\overline{w}\cdot Ke_z\right)+\left(\overline{V'\cdot\nabla Ke+w'\cdot Ke_z}\right)$$
$$=-\overline{V'\nabla P'}-\rho_0\overline{V'\left(V'\cdot\nabla\overline{V}+w'\cdot\overline{V}_z\right)}+\rho_0\overline{V'\left(V'\cdot\nabla V'+w'\cdot V_z'\right)} \tag{A4}$$

Here, the terms on the left side of eq.(A4) are the local tendency, the total advection by mean flow, and the total advection by eddies of K_e. On the right side, the first term is the pressure work done by eddies, the second term is the horizontal and vertical deformation work term, and the third term is zero over the time mean. The horizontal deformation work terms in eq.(A4) using northward and eastward component velocities of (u_n',u_e') can be expressed by

$$N'=-\overline{V'\left(V'\cdot\nabla\overline{V}\right)}$$
$$=-\left[\overline{u_e'u_e'}\frac{\partial\overline{u_e}}{\partial x}+\overline{u_e'u_n'}\left(\frac{\partial\overline{u_e}}{\partial y}+\frac{\partial\overline{u_n}}{\partial x}\right)+\overline{u_n'u_n'}\frac{\partial\overline{u_n}}{\partial y}\right. \tag{A5}$$

When $N'>0$, it represents the conversion from mean kinetic energy K_M into eddy kinetic energy K_e (Wells and Ivchenko, 2000). This energy transfer is due to the work of Reynolds

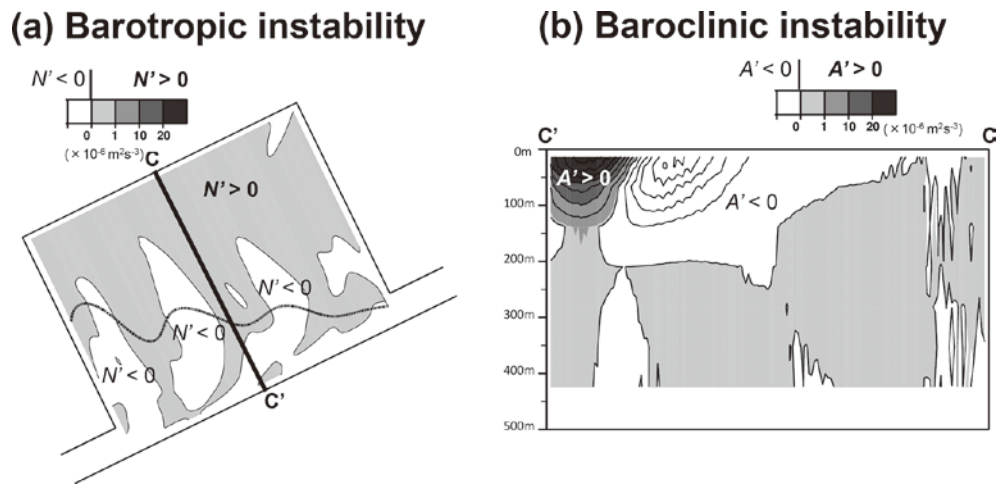

Fig. A1. (a) Horizontal distribution for the energy transfer term N' at the sea surface and (b) vertical distribution for the energy transfer term A' across the central section C–C' in (a). They were calculated from the model results over a one-year period. The region with positive sign of N' in (a) and A' in (b), respectively, corresponds to the occurrence of barotropic and baroclinic instabilities.

stresses against the horizontal shear of mean flow. Such energy transfer is commonly referred to as "barotropic instability". Conversely, when $N' < 0$, there is an exchange from K_e to K_M, and eddies act to strengthen the mean flow.

The equation for eddy potential energy $P_e = -\frac{g}{2\tilde{\rho}_z}\overline{\rho'\rho'}$ (Oort and Ascher, 1989) is given by

$$\frac{\partial Pe}{\partial t} + \left(\overline{V}\cdot\nabla Pe + \overline{w}\cdot Pe_z\right) + \left(\overline{V'\cdot\nabla Pe + w'\cdot Pe_z}\right) = -g\overline{\rho' w'} - \frac{g}{\tilde{\rho}_z}\overline{\rho'\left(V'\cdot\nabla\overline{\rho}\right)} + \frac{g}{\tilde{\rho}_z}\overline{\rho'\left(\overline{V'\cdot\nabla\rho' + w'\cdot\rho'_z}\right)} \quad \text{(A6)}$$

where $\tilde{\rho}$ is the horizontal averaged density distribution over the time mean. The terms on the left side of eq.(A6) are the local tendency, the total advection by mean flow, and the total advection by eddies of P_e. The first (called B') and second (called A') terms on the right side of eq.(A6) are the energy transfer between P_e and K_e, and the third term is zero over the time mean. The energy transfer term B' is locally strongly modified by upwelling and downwelling. Since the transfer term B', which involves vertical velocity, is strongly influenced by flow over the rough bottom topography, this term may not give a reliable indication of local instability processes according to Beckmann and Boning (1994). Therefore, only the transfer term A' was examined as an indication of the "baroclinic instability" to understand the eddy-generating mechanisms, i.e.,

$$A' = -\frac{g}{\tilde{\rho}_z}\overline{\rho'\left(V'\cdot\nabla\overline{\rho}\right)} = -g\frac{\overline{u_e'\rho'}\frac{\partial\overline{\rho}}{\partial x} + \overline{u_n'\rho'}\frac{\partial\overline{\rho}}{\partial y}}{\frac{\partial\overline{\tilde{\rho}}}{\partial z}} \quad \text{(A7)}$$

When $A' > 0$, corresponding to the "baroclinic instability", it represents the transfer from mean potential energy P_M to eddy potential energy P_e.

The energy transfer term N' is much smaller than the transfer term A', so the energy transfer due to the barotropic instability is less dominant (Fig. A1(a)). The baroclinic instability with $A' > 0$ is limited only to the upper southern boundary, where a strong upwelling exists year round. Since the offshore surface region always has $A' < 0$ (Fig. A1(b)), we think that the genesis for meandering cannot be explained by both baroclinic and barotropic instabilities.

Appendix B : Dispersion relation of standing Rossby wave

A two-layer model under the eastward flow on the planetary-β plane (Fig. A2) is considered to be a better interpretation for the meandering as standing Rossby waves. Based on the annual mean state in our CIC model, the meridional width of the TWC region is L = 500 km, the mean thickness of the upper layer is H_m = 200 m, and the full depth of the model is D = 500 m. The meridional averaged surface velocity of eastward meandering flow (U) is given as 2.2 cm s^{-1}. In the liner theory, U is considered as an external force in the geostrophic current as follows :

$$fU = g^* \frac{dH_1}{dy} \quad \text{(A8)}$$

where g^* = 0.03 m s^{-2} is the annual mean reduced gravity, H_1 is inclined upper layer due to the geostrophic flow U. The values of the Coriolis parameter f_0 and planetary β are the same as those in the numerical model. The linearized vorticity equations in the upper and lower layers under the quasi-geostrophic approximation expressed by the pressure anomalies of P_1' and P_2', are given by

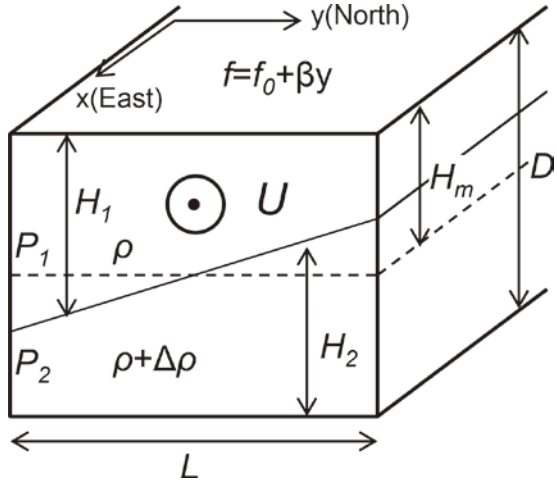

Fig. A2. Schematic view of two-layer analytic model on the planetary-β plane with a constant eastward surface flow U. The meridional section of interface accompanied by the eastward flow of U is depicted.

$$\left(\frac{\partial}{\partial t}+U\frac{\partial}{\partial x}\right)\left(\nabla^2 P_1'-\lambda_1^{-2}\left(P_1'-P_2'\right)\right)+\left(\beta+\lambda_1^{-2}U\right)\frac{\partial P_1'}{\partial x}=0 \tag{A9}$$

$$\frac{\partial}{\partial t}\left(\nabla^2 P_2'+\lambda_2^{-2}\left(P_1'-P_2'\right)\right)+\left(\beta-\lambda_2^{-2}U\right)\frac{\partial P_2'}{\partial x}=0 \tag{A10}$$

where $\lambda_1=\sqrt{g^* H_m}\ /\ f_0$ and $\lambda_2=\sqrt{g^*\left(D-H_m\right)}\ /\ f_0$ are the internal deformation radius of upper and lower layers, respectively. The solutions of P_1' and P_2' have the following forms

$$P_1'=A\sin\left(\frac{\pi y}{L}\right)e^{i(kx-\sigma t)} \qquad P_2'=B\sin\left(\frac{\pi y}{L}\right)e^{i(kx-\sigma t)} \tag{A11}$$

where k is the east-west wave number, and σ is the frequency. The constant values of A and B are the upper and lower disturbance amplitudes, respectively. From eqs.(A9) to (A11), the dispersion relations are given by

$$\sigma_+=\frac{-B+\sqrt{\Delta}}{2A} \qquad \sigma_-=\frac{-B-\sqrt{\Delta}}{2A} \tag{A12}$$

$$A=l^2\left(l^2+\lambda_1^{-2}+\lambda_2^{-2}\right) \tag{A13}$$

$$B=\left[k\beta\left(2l^2+\lambda_1^{-2}+\lambda_2^{-2}\right)-k^2\beta U l^2\left(l^2+2\lambda_1^{-2}\right)\right] \tag{A14}$$

$$\Delta=k^2\beta^2\left[\left(\lambda_1^{-2}+\lambda_2^{-2}\right)^2\right]+k^2U^2l^4\left(l^4-4\lambda_1^{-2}\lambda_2^{-2}\right)+2k^2U\beta l^4\left(\lambda_1^{-2}-\lambda_2^{-2}\right) \tag{A15}$$

$$l^2=k^2+\left(\frac{2\pi}{L}\right)^2 \tag{A16}$$

Here, when $\Delta\geq 0$, $\sigma_+(k)$ and $\sigma_-(k)$ are independent frequencies in the surface-trapped and bottom-trapped disturbances. If $\Delta\leq 0$, the solution has a one-frequency including the imaginary part, i.e., the baroclinic instability wave.

Acknowledgments

We are deeply indebted to Mr. Keijirou Asahi of Hitachi, Ltd. for his support in the analytical approach shown in Appendix B. We thank Dr. Satoshi Nakada of the National Institute for Environmental Studies, Japan for his useful comments concerning the lateral heat transport in the Japan Sea, Dr. John Bower of Hokkaido University for his English proofreading of our manuscript, and specially-appointed Prof. Sei-ichi Saitoh of Hokkaido University for the AVHRR data in Fig. 1(a). This paper is based on the master's thesis of the first author (Fang, 2014), but includes additional results and discussion.

References

Asahi, K., Isoda, Y. and Fang, X. (2016) Seasonal changes of sea surface height and sea surface geostrophic current anomalies in the Japan Sea. *Oceanography in Japan*, **25**(3), 43-61. (in Japanese with English abstract)

Asahi, K. and Isoda, Y. (2017) Influence of topographic β-effect upon seasonal variation of wind-driven circulation in the Japan Sea. *Bull. Fish. Sci. Hokkaido Univ.*, **67**(3), 39-55. (in Japanese with English abstract)

Beckmann, A. and Boning, C.W. (1994) On the generation and role of eddy variability in the central North Atlantic Ocean. *J. Geophy. Res.*, **99**(C10), 381-391.

Blumberg, A.F. and Mellor, G.L. (1987) A description of a three-dimensional coastal ocean circulation model. pp. 1-16, Heaps, N. (ed.), *Three-Dimensional Coastal Ocean Models*, Vol. 4, American Geophysical Union, Washington, D.C.

Fang, X. (2014) Dynamic equilibrium state of Cooling Induced Current in the Japan Sea. *Master's thesis, Hokkaido University, Graduate School of Fisheries Sciences*.

Gamo, T., Momoshima, N. and Tolmachyov, S. (2001) Recent upward shift of the deep convection system in the Japan Sea, as inferred from the geochemical tracers, tritium, oxygen, and nutrients. *Geophys. Res. Lett.*, **28**, 4143-4146.

Gamo, T. (2014) Excess ^{222}Ra profiles in the bottom layer of the Japan Sea and their implication for bottom water dynamics. *Prog. Oceanogr.*, **121**, 94-97.

Han, S., Hirose, N. and Kida, S. (2018) The role of topographically induced form drag on the channel flows through the East/Japan Sea. *J. Geophys. Res.*, 10.1029/2018JC 013903.

Higaki, H., Isoda, Y., Isogai, Y. and Yahaba, Y. (2008) Seasonal variations of water system distributions and flow patterns off the west coast of Hokkaido. *Oceanography in Japan*, **17**(4), 223-240. (in Japanese with English abstract)

Hirose, N., Kim, C.H. and Yoon, J.H. (1996) Heat budget in the Japan Sea. *J. Oceanogr.*, **52**, 553-574.

Holloway, G., Sou, T. and Eby, M. (1995) Dynamics of circulation of the Japan Sea. *J. Mar. Res.*, **53**, 539-569.

Ida, S., Yamashita, S, Isoda, Y. and Kobayashi, N. (2016) Inflow process of low potential vorticity water originating from the intermediate waters of the Japan Sea into the Tsugaru Strait. *Oceanography in Japan*, **25**(4), 101-122. (in Japanese with English abstract)

Iida, H., Isoda, Y., Kobayashi, N. and Horio, K. (2018) Observations and model experiments of the diurnal eddy of the Cold Water Belt along the offshore side of the Soya Warm Current.

Oceanography in Japan, **27**(4), 155–174. (in Japanese with English abstract)

Iino, R., Isoda, Y. and Yahaba, H. (2009) Sea level difference inducing the passage–flow through the Tsugaru Strait. *Umi to Sora*, **85**(1), 1–19. (in Japanese with English abstract)

Ishikawa, K., Isoda, Y. and Aiki, T. (2007) Seasonal variation in the nearshore branch of the Tsushima Warm Current as inferred form coastal sea level data. *Oceanography in Japan*, **16**(3), 223–236. (in Japanese with English abstract)

Isobe, A. and Isoda, Y. (1997) Circulation in the Japan Basin, the northern part of the Japan Sea. *J. Oceanogr.*, **53**, 373–381.

Isoda, Y., Saitoh, S. and Mihara, M. (1991) SST structure of the polar front in the Japan Sea. pp. 103–112, Takano, K. (ed.), *Oceanography of Asian Marginal Seas*,Vol.54, Elsevier.

Isoda, Y. and Nishihara, M. (1992) Behavior of warm eddies in the Japan Sea. *Umi to Sora*, **67**, 231–243. (in Japanese with English abstract)

Isoda, Y., Saitoh, S. and Mihara, M. (1992a) Seasonal variations of SST patterns in the Japan Sea. *Umi to Sora*, **68**(3), 113–124. (in Japanese with English abstract)

Isoda, Y., Naganobu, M., Watanabe, H. and Nukata, K. (1992b) Horizontal and vertical structures of a warm eddy above the Yamato Rise. *Oceanography in Japan*, **1**(4), 141–151. (in Japanese with English abstract)

Isoda, Y. and Saitoh, S. (1993) The northward intruding eddy along the east coast of Korea. *J. Oceanogr.*, **49**, 443–458.

Isoda, Y. (1994a) Warm eddy movements in the eastern Japan Sea. *J. Oceanogr.*, **50**, 1–15.

Isoda, Y. (1994b) Interannual SST variations to the north and south of the polar front in the Japan Sea. *La mer*, **32**, 285–293.

Isoda, Y. and Korematsu, H. (1995) Interannual variations of water temperature, salinity and oxity vertical distributions in the Tsushima Current region. *Umi to Sora*, **71**(2), 47–57. (in Japanese with English abstract)

Isoda, Y. (1996) Interaction of a warm eddy with the coastal current at the eastern boundary area in the Tsushima Current region. *Conti. Shelf Res*., **16**(9), 1149–1163.

Isoda, Y. and Kim, S.W. (1998) Interannual variations of the surface mixed layer in the Tsushima Current region. *Umi to Sora*, **74**(1), 11–22. (in Japanese with English abstract)

Isoda, Y. and Tanaka, K. (1999) Interannual variations of bifurcation of the Tsushima Warm Current around the Tsushima/Korea Strait. *Umi to Sora*, **75**(3), 71–79. (in Japanese with English abstract)

Isoda, Y. (1999) Cooling–induced Current in the upper ocean of the Japan Sea. *J. Oceanogr.*, **55**, 585–596.

Isoda, Y. (2003) Formation of abyssal waters and polar front in the Japan Sea inferred from the route of heat transport. *Oceanography in Japan*, **12**(1), 69–84. (in Japanese with English abstract)

Isoda, Y. (2004) Tsushima Current Mode Water (TCMW). *Bull. Fish. Sci. Hokkaido Univ.*, **55**(2), 75–83.

Isoda, Y. (2011) Climate change and physical process associated with the Tsushima Warm Current. *Mem. Fac. Fish. Sci. Hokkaido Univ.*, **53**(2), 2–12. (in Japanese with English abstract)

Iwasaka, N. and Hanawa, K. (1990) Climatologies of marine meteorological variables and surface fluxes in the North Pacific computed from COADS. *Tohoku Geophysical Journal*, **33**, 185–239.

Jacobs, G.A., Hogan, P.J. and Whitmer, K.R. (1999) Effects of eddy variability on the circulation of the Japan/East Sea. *J. Oceanogr.*, **55**, 247–256.

Kang, D.J., Park, S., Kim, Y.G., Kim, K. and Kim, K.R. (2003) A moving–boundary box model (MBBM) for oceans in change : Application to the East/Japan Sea. *Geophys. Res. Let.*, **30**, doi : 10.10129/2002GL016486.

Kato, K. and Asai, T. (1983) Seasonal variations of heat budgets in both the atmosphere and the sea in the Japan Sea. *J. Meteor. Soc. Japan*, **61**, 222–238.

Kawabe, M. (1982) Branching of the Tsushima Current in the Japan Sea Part II. Numerical experiment. *J. Oceanogr. Soc. Japan*, **38**, 183–192.

Kida, S., Qiu, B., Yang, J. and Lin, X. (2016) The annual cycle of the Japan Sea throughflow. *J. Phys. Oceanogr.*, **46**(1), 23–39.

Kim, C.H. and Yoon, J.H. (1996) Modeling of the wind–driven circulation in the Japan Sea using a reduced gravity model. *J. Oceanogr*., **52**, 359–373.

Kim, C.H. and Yoon, J.H. (1999) A numerical modeling of the upper and the intermediate layer circulation in the East Sea. *J. Oceanogr.*, **55**, 327–345.

Kim, K., Kim, K.R., Kim, Y.G., Cho, Y.K., Kang, D.J., Takematsu, M. and Volkov, Y. (2004) Water masses and decadal variability in the East Sea (Sea of Japan). *Prog. Oceanogr.*, **61**, 157–174.

Kim, K.J. and Seung, Y.H. (1999) Formation and movement of the ESIW as modeled by MICOM. *J. Oceanogr*., **55**, 369–382.

Kuma, K., Sasayama, R., Hioki, N., Morita, Y., Isoda, Y., Hirawake, T., Imai, K., Aramaki, T., Nakamura, T., Nishioka, J. and Ebuchi, N. (2014) Chemical evidence for the origin of the cold water belt along the northeastern coast of Hokkaido. *J. Oceanogr.*, **70**, 377–387.

Kumamoto, Y., Aramaki, T., Watanabe, S., Yoneda, M., Shibata, Y., Togawa, O., Morita, M. and Shitashima, K. (2008) Temporal and spatial variations of radiocarbon in Japan Sea Bottom Water. *J. Oceanogr*., **64**, 429–441.

Lee, D.K., Niiler, P.P., Lee, S.R., Kim, K. and Lie, H.J. (2000) Energetics of the surface circulation of the Japan/East Sea. *J. Geophys. Res.*, **105**(C8), 19561–19573.

Masina, S., Philander, S.G.H. and Bush, A.B.G. (1999) An analysis of the tropical instability waves in a numerical model of the Pacific Ocean 2. Generation and energetics of the waves. *J. Geophy. Res.*, **104**(C12), 637–661.

Matsuoka, S., Fang, X. and Isoda, Y. (2019) High–Salinity Intermediate Water in the eastern Japan Sea. *Bull. Fish. Sci. Hokkaido Univ.*, **69**(2), 71–82. (in Japanese with English abstract)

Minato, S. and Kimura, R. (1980) Volume transport of the Western Boundary Current penetrating into a marginal sea. *J. Oceanogr. Soc. Japan*, **36**, 185–195.

Mori, K., Isoda, Y. and Shimizu, M. (2006) Interannual variation of water temperature and salinity in deep water west of the Tsugaru Strait. *Rep. Inst. Appl. Mech. Kyushu Univ.*, **130**, 1–10. (in Japanese with English abstract)

Morie, R., Isoda, Y., Fujiwara, S. and Fang, X. (2015) The contribution of standing Rossby waves to the development of the Tsushima Warm Current–meandering. *Oceanography in Japan*, **24**(1), 29–47. (in Japanese with English abstract)

Na, J., Seo, J. and Lie, H.J. (1999) Annual and seasonal variations of the sea surface heat fluxes in the East Asian marginal seas. *J. Oceanogr*., **55**, 257–270.

Nakada, S., Isoda, Y. and Kusahara, K. (2002) Response of the coastal branch flow to alongshore variation in shelf topography off Toyama Bay. *Oceanography in Japan*, **11**(2), 243–258. (in Japanese with English abstract)

Nakajima, Y., Isoda, Y., Matsuura, H., Wagawa, T., Aiki, T., Yabe, I., Takata, H., Kuma, K., Kobayashi, N. and Yahaba, H. (2008) Tsushima Warm Current water inflow to Tsugaru Strait. *Umi to Sora*, **84**(1), 1–16. (in Japanese with English abstract)

Nof, D. (2000) Why much of the Atlantic circulation enters the Caribbean Sea and very little of the Pacific circulation enters the Sea of Japan. *Prog. Oceanogr.*, **45**, 39–67.

Ohshima, K.I. (1994) The flow system in the Japan Sea caused by a sea level difference through shallow straits. *J. Geophys. Res.*, **99**, 9925–9940.

Oort, A.H. and Ascher, S.C. (1989) New estimates of the available potential energy in the world ocean. *J. Geophy. Res.*, **94**(C3), 3187–3200.

Seung, Y.H. (2003) Significance of shallow bottom friction in the dynamics of the Tsushima Current. *J. Oceanogr.*, **59**, 113–118.

Seung, Y.H. and Kim, K.J. (2011) Boundary currents in a meridional channel subject to seasonally varying buoyancy forcing : application to the Tsushima Current. *J. Oceanogr.*, **67**, 563–575.

Spall, M.A. (2002) Wind- and buoyancy-forced upper ocean circulation in two-strait marginal seas with application to the Japan/East Sea. *J. Geophys. Res.*, **107**, 1029–2001.

Stommel, H. (1948) The westward intensification of wind-driven ocean currents. *Trans. Amer. Geoph. Union*, **29**, 202–206.

Takamasu, A., Isoda, Y. and Asahi, K. (2019) Extraction of cooling-induced current from the satellite sea surface height anomaly in the Japan Sea. *Bull. Fish. Sci. Hokkaido Univ.*, **69**(1), 19–28. (in Japanese with English abstract)

Takikawa, T. and Yoon, J.H. (2005) Volume transport through the Tsushima Straits estimated from sea level difference. *J. Oceanogr.*, **61**, 699–708.

Tsujino, H., Nakano, H. and Motoi, T. (2008) Mechanism of currents through the straits of the Japan Sea : Mean state and seasonal variation. *J. Oceanogr.*, **64**, 141–161.

Wells, N.C. and Ivchenko, V.O. (2000) Instabilities in the Agulhas retroflection current system : A comparative model study. *J. Geophy. Res.*, **105**(C2), 3233–3241.

Yoon, J.H. (1982a) Numerical experiment on the circulation in the Japan Sea Part I. Formation of the East Korean Warm Current. *J. Oceanogr. Soc. Japan*, **38**, 43–51.

Yoon, J.H. (1982b) Numerical experiment on the circulation in the Japan Sea Part II. Influence of seasonal variations in atmospheric conditions on the Tsushima Current. *J. Oceanogr. Soc. Japan*, **38**, 81–94.

Yoshikawa, Y., Awaji, T. and Akitomo, K. (1999) Formation and circulation processes of intermediate water in the Japan Sea. *J. Phys. Oceanogr.*, **29**, 1701–1722.